Geosci. Model Dev. Discuss., 8, 10735–10781, 2015
www.geosci-model-dev-discuss.net/8/10735/2015/
doi:10.5194/gmdd-8-10735-2015

Geoscientific Model Development Discussions
Open Access
EGU

Coupling aerosol optics to the chemical transport model MATCH (v5.5.0) and aerosol dynamics module SALSA (v1)

E. Andersson[1] **and M. Kahnert**[1,2]

[1]Department of Earth and Space Sciences, Chalmers University of Technology, 41296 Gothenburg, Sweden
[2]Swedish Meteorological and Hydrological Institute, 60176 Norrköping, Sweden

Received: 3 November 2015 – Accepted: 2 December 2015 – Published: 21 December 2015

Correspondence to: M. Kahnert (michael.kahnert@smhi.se)

Published by Copernicus Publications on behalf of the European Geosciences Union.

Abstract

Modelling aerosol optical properties is a notoriously difficult task due to the particles' complex morphologies and compositions. Yet aerosols and their optical properties are important for Earth system modelling and remote sensing applications. Operational optics models often make drastic and non realistic approximations regarding morphological properties, which can introduce errors. In this study a new aerosol optics model is implemented, in which more realistic morphologies and mixing states are assumed, especially for black carbon aerosols. The model includes both external and internal mixing of all chemical species, it treats externally mixed black carbon as fractal aggregates, and it accounts for inhomogeneous internal mixing of black carbon by use of a novel "core-grey shell" model. Simulated results of radiative fluxes, backscattering coefficients and the Ångström exponent from the new optics model are compared with results from another model simulating particles as externally mixed homogeneous spheres. To gauge the impact on the optical properties from the new optics model, the known and important effects from using aerosol dynamics serves as a reference. The results show that using a more detailed description of particle morphology and mixing states influences the optical properties to the same degree as aerosol dynamics. This is an important finding suggesting that over-simplified optics models coupled to a chemical transport model can introduce considerable errors; this can strongly effect simulations of radiative fluxes in Earth-system models, and it can compromise the use of remote sensing observations of aerosols in model evaluations and chemical data assimilation.

1 Introduction

Aerosol optics models are employed in large-scale chemical transport models (CTMs) in mainly two contexts, namely, in Earth-system climate modelling, and in conjunction with remote sensing observations. In Earth-system modelling one couples a CTM to

GMDD
8, 10735–10781, 2015

an atmosphere-ocean general circulation model (GCM). One purpose is to account for the dynamic effects of aerosols on cloud microphysics. Another is to obtain a better description of the direct effect of aerosols and radiatively active trace gases on the radiative balance. The aerosol optics model provides a link that converts the aerosol fields delivered by the CTM to the aerosol optical properties that are required as input to the radiative transfer model, with which one computes the radiative energy budget. In remote sensing applications one is faced with the obstacle that the aerosol concentration fields computed with a CTM are not directly comparable to the radiometric quantities that are observed with remote sensing instruments. The aerosol optics model provides the observation operator that maps the CTM output to radiometric variables that can be compared to satellite observations or satellite retrieval products. This allows us to either employ satellite observations for evaluating CTM model results, or to assimilate satellite data into a CTM-based air-quality forecasting system. It is clear that the aerosol optics model has a pivotal role in these kinds of applications. It may constitute an additional source of error that could compromise the reliability of Earth-system climate models, impair the reliability of CTM evaluations, or degrade chemical data assimilation results. It is, therefore, important to better understand this potential source of error, quantify its possible impact on model predictions of aerosol radiometric quantities, and assess the level of morphological detail that is required in aerosol optics models coupled to CTMs.

A main difficulty is that aerosols in nature can have a high degree of morphological complexity. For instance, mineral dust particles can have irregular shape, small-scale surface roughness, and inhomogeneous mineralogical composition (e.g. Nousiainen, 2009). Black carbon aerosols are fractal aggregates (e.g. Jones, 2006) that can be coated by weakly absorbing liquid-phase components that condense onto the aggregates as they age in the atmosphere (e.g. Adachi and Buseck, 2008). Volcanic ash particles are composed of crustal material in which multiple air vesicles may have been trapped during the generation of the particles. In aerosol optics models one has to

GMDD
8, 10735–10781, 2015

make a choice what level of morphological detail is necessary and affordable. A detailed discussion of this question can be found in Kahnert et al. (2014).

In environmental modelling practical and computational constraints often force us to invoke drastically simplifying assumptions about aerosol morphology. For instance, one frequently computes aerosol optical properties based on the assumption that all chemical aerosol components are contained in separate particles, and that each such particle can be approximated as a homogeneous sphere. As pointed out in Kahnert (2008); Benedetti et al. (2009), this approach is highly attractive from a practical point of view, because the aerosol optical observation operators, which map mixing ratios to radiometric properties, become linear functions of the mixing ratios of the different chemical species. A linearisation of the observation operator is a prerequisite for most of the commonly used data assimilation methodologies, such as the variational method (e.g. Kahnert, 2008; Benedetti et al., 2009). However, such approximations can also introduce substantial errors. In the remote sensing community awareness for this problem has been growing over the past 1–2 decades. As a result, one has developed retrieval methods for desert dust aerosols that are based on spheroidal model particles (e.g. Dubovik et al., 2006), which can mimic the optical properties of mineral dust particles better than homogeneous spheres Kahnert (2004); Nousiainen et al. (2006). In chemical data assimilation, the problem is still treated rather negligently. A few assimilation studies account for internal mixing of different chemical components (e.g. Saide et al., 2013). But the particles are still assumed to be perfectly homogeneous spheres. To the best of our knowledge there are currently no aerosol optical observation operators in chemical transport models that take complex morphological properties of aerosols such as nonsphericity or inhomogeneous internal structure into account.

This study describes the coupling of two different aerosol optics models to a regional CTM. One optics model is based on the simple external-mixture and homogeneous-sphere approximations. The second model takes both external and internal mixing of aerosol components into account. Also, it employs morphologically more realistic models for black carbon aerosols. Although black carbon contributes, on average, only

GMDD
8, 10735–10781, 2015

some 5 % to the mass mixing ratio of particulate matter over Europe, it can have a significant global radiative warming effect. Previous theoretical studies on the optical properties of black carbon aerosols suggest that the use of homogeneous sphere models can introduce substantial errors in the absorption cross section and single scattering albedo of such particles (e.g. Kahnert, 2010a; Kahnert et al., 2013). The main goal of this study is to assess the impact of aerosol morphology and mixing state on radiometric quantities and radiative forcing rates simulated with a chemical transport model. To this end we compare the two optics models, and we gauge the significance of morphology by comparing the differences in the optics models to other sources of error. As a gauge we use the impact of including or omitting aerosol dynamic processes; this provides us with a reference which is generally agreed to have a significant effect on aerosol transport models.

The CTM, its aerosol dynamics and mass transport modules, and the aerosol optics model are described in Sect. 2. There we also explain the methodology we employ for evaluation of the optics model. In Sect. 3 we present and discuss computational results for selected cases and for several radiative and optical parameters. Concluding remarks are given in Sect. 4.

2 Model description and methods

2.1 General considerations and terminology

Aerosol particles typically originate from different emission sources, such as seasalt particles coming from marine sources, wind-blown dust from dry land surfaces, volcanic ash from magmatic or phreatomagmatic eruptions, or black carbon produced during combustion of fossil fuel, biofuel, or biomass. During atmospheric transport particles from different sources can be mixed, resulting in heterogeneous aerosol populations consisting of particles of different morphologies, sizes, and chemical composition. A mixture in which different chemical species are contained in separate particles is re-

GMDD
8, 10735–10781, 2015

ferred to as an *external mixture*. On the other hand, aerosol dynamic processes, such as nucleation, condensation, and coagulation, give rise to the formation and growth of secondary particles from precursor gases, as well as to the condensation of precursor gases onto existing primary particles. These processes result in particles in which several chemical species are mixed with each other in one and the same particle. Such a population is referred to as an *internal mixture*. There are two types of internal mixtures. If, e.g., hydrophillic liquid-phase components mix with each other, one can obtain a *homogeneous internal mixture* of different chemical species. On the other hand, condensation of gas-phase species onto non-soluble primary particles, or cloud processing of aerosols can result in liquid-phase material coating a solid core of, e.g., mineral dust or black carbon. We refer to the latter as an *inhomogeneous internal mixture*. Aerosol populations in nature are often both externally and internally mixed, i.e., they contain particles that are composed of a single chemical species as well as other particles that are composed of different chemical species, which can be homogeneously or inhomogeneously internally mixed.

Aerosol optical properties are strongly dependent on not only the size and chemical composition, but also on the mixing state, shape, and internal structure of particles. Therefore, before explaining the aerosol optics model, we first need to briefly describe the kind of information that can be provided by the aerosol transport model. In particular, we need to understand the level of detail with which the size distribution, size-dependent chemical composition, and the mixing state of the aerosols can be computed in a large-scale model.

2.2 Aerosol transport modelling with MATCH

As a regional model we employ the Multiple-scale Atmospheric Transport and CHemistry modelling system (MATCH) Andersson et al. (2007). The MATCH model allows us to choose between two aerosol model versions, a simpler mass transport model, and a more sophisticated aerosol dynamic transport model.

GMDD
8, 10735–10781, 2015

2.2.1 Mass transport model

A simple version, which we refer to as the "mass transport model", neglects all aerosol dynamic processes. It contains a photochemistry model that computes mass concentrations of secondary inorganic aerosols (SIA), which are formed from precursor gases. The SIA fraction consists of ammonium sulphate ($(NH_4)_2SO_4$), ammonium nitrate (NH_4NO_3), other particulate sulphates (PSO_x), and other particulate nitrates (PNO_x). The mass transport model further contains a seasalt module that computes NaCl emissions based on the parametrisations described in Mårtensson et al. (2003); Monahan et al. (1986). It also contains a simple wind-blown dust model and a module for transport of primary particulate matter (PPM), i.e., aerosols other than seasalt and windblown dust that are emitted as particles, rather than being formed from gas precursors. The size bins in the PPM model are flexible. In the current model set-up the sea salt and PPM models were run for four size bins as shown in Table 1. We used EMEP PPM emission data for the year 2007, and, based on those and on Kupiainen and Klimont (2004, 2007), we generated gridded emission data for black carbon (BC), organic carbon (OC), and all other PPM. (Here, OC refers to the mass of all organic matter, not just the mass of carbon atoms in organic compounds.) The primary particle emissions are distributed among the four size classes; during atmospheric transport they remain chemically and dynamically inert in the model. Thus no chemical transformation, mixing processes with other compounds, or other size transformation processes are included in the model. The SIA components are given as total mass concentrations without any information about their size distribution. In the optics model a fixed size distribution is assumed to assign the total SIA mass to the four size bins.Water adsorption by particles is computed in the optics model as described in Sect. 2.3.1. More details on the MATCH photochemistry model can be found in Robertson et al. (1999); Andersson et al. (2007). The MATCH seasalt model is described in Foltescu et al. (2005).

GMDD
8, 10735–10781, 2015

2.2.2 Aerosol dynamics model

A more realistic description of particles can be achieved by accounting for aerosol dynamic processes. To this end the Sectional Aerosol module for Large Scale Applications (SALSA) (Kokkola et al., 2008) has recently been coupled to the MATCH photochemistry model (Andersson et al., 2015). The description of PNO_x, wind-blown dust, and secondary organic aerosols (SOA) is still under development in MATCH-SALSA. A simplified PNO_x description has been included in the model version employed here, while wind-blown dust and SOA are absent. The number and range of size bins is flexible in SALSA. Table 2 shows the current model set-up.

As is evident from the table, MATCH-SALSA accounts for both internally and externally mixed aerosols. For instance, size bins 12, 15, and 18 describe the same size range (350–873 nm), but different internal mixtures of various species. Similarly, bins 4 and 8 have the same size range (25–49 nm), but one describes an internal mixture, the other an external mixture of aerosol species.

Note that water is not directly calculated as a prognostic variable in MATCH-SALSA. Rather, it is a diagnostic variable computed in the MATCH-optics model as explained in Sect. 2.3.2. The table merely indicates which size bins are assumed in the optics model to be internally mixed with adsorbed water. A more detailed description of the MATCH-SALSA model can be found in Andersson et al. (2015).

2.3 Aerosol optics modelling

Aerosol optics models coupled to a CTM have to make consistent use of the information provided by the CTM, while invoking assumptions on optically relevant parameters that are not provided by the CTM. The parameters that influence the particles' optical properties are

- the aerosol size distribution;
- the refractive index of the materials of which the aerosols are composed;

GMDD
8, 10735–10781, 2015

– the morphology of the particles.

Morphology refers to both the overall shape of the particle, and, in case of inhomogeneously mixed particles, the variation of the refractive index inside the particle.

The information provided by the CTM depends on the level of detail in the process descriptions. In the MATCH mass transport model, we have size information for the primary particles, but only the total mass for secondary inorganic aerosols. Thus we have to invoke assumptions about the size distribution of these particles. The MATCH optics models in conjunction with the MATCH mass transport model assume that 10 % of the SIA aerosol mass are in the smallest size class (see Table 1), 60 % in the second, 20 % in the third, and 10 % in the fourth size class. Also, the mass transport model lacks any information about the mixing state of the particles. We therefore have to invoke appropriate assumptions on whether the aerosols are externally or internally mixed. Both the mass transport model and MATCH-SALSA lack information on whether the internally mixed particles are homogeneous or inhomogeneous. Also, neither model provides any information on the shape of the particles. The refractive index of the different chemical components in the aerosol phase and their spectral variation is given in Fig. 4 of Kahnert (2010a). That reference also contains detailed information about the different literature sources from which the refractive indices are taken.

2.3.1 Optics model for externally mixed aerosols

The simplest conceivable optics model assumes that all particles are homogeneous spheres, and that all chemical species are each in separate particles, i.e., externally mixed. As explained in Kahnert (2008), the external-mixture assumption results in a linear relation between the mass mixing ratios and the optical properties. Owing to the linearity, this model is particularly attractive for data assimilation applications (e.g. Benedetti et al., 2009), which require linearised observation operators. However, this is also the crudest possible optics model, as it neglects both the effect of internal mixing and of particle morphology on optical properties.

GMDD
8, 10735–10781, 2015

The external-mixture model is implemented in the MATCH mass transport model, where it is primarily being used in the MATCH 3DVAR data assimilation system Kahnert (2008). Optical properties are pre-computed for twelve wavelength bands ranging from the UV-C to the mid-IR. Dust and black carbon are assumed to be hydrophobic, while sea salt, OC, and SIA components can each mix internally with water. The water volume fraction depends on temperature and humidity; it is computed by use of the parametrisation given in Gerber (1985). The aerosol/water mixture is assumed to be homogeneous. The dielectric properties of a homogeneous mixture of two or more components are described by a complex effective refractive index m_{eff}, which is usually computed by effective medium theory (EMT) (although chemical transport modellers often use simple volume mixing rules, most likely because EMTs are not commonly known in that field). We use Bruggemann's EMT (Bruggemann, 1935). Optical properties are pre-computed for eleven water volume fractions between 0 and 0.98; for intermediate volume fractions the optical properties are interpolated. The optical properties contained in the database are the extinction cross section C_{ext}, the scattering cross section C_{sca}, the value of the phase function in the exact backscattering direction $p(180^{\circ})$, and the asymmetry parameter g.

As explained in Kahnert (2008), size-averaged optical properties are pre-computed by averaging over a log-normal size distribution $n_i(r) = N_i/(\sqrt{2\pi}r\ln\sigma_i)\exp[-\ln^2(r/r_i)/(2\ln^2\sigma_i)]$ for each size class i, where N_i represents the number density of particles in size bin i, r denotes the particle radius, $r_1 = 0.022\,\mu\text{m}$, $r_2 = 0.158\,\mu\text{m}$, $r_3 = 0.791\,\mu\text{m}$, $r_4 = 2.5\,\mu\text{m}$ are the mean radii in each size mode, and the variances $\sigma_1 = \sigma_3 = \sigma_4 = 1.8$, $\sigma_2 = 1.5$ are based on measurements in Neusüß et al. (2002). The volume per size bin can be obtained by integrating $(4/3)\pi r^3 n_i(r)$ over the ith size bin interval; this can be used for converting mass mixing ratios into number densities in each size bin, which, in turn, allows us to compute radiative properties, such as aerosol optical depth (AOD), single-scattering albedo (SSA), asymmetry parameter g, and backscattering coefficient β_{bak} in each atmospheric grid cell in MATCH – see Kahnert (2008) for details.

GMDD
8, 10735–10781, 2015

2.3.2 Optics model for aerosols of different mixing states

The new MATCH-optics model accounts for both internally and externally mixed aerosols, and it contains both homogeneously and inhomogeneously mixed aerosols. Different shapes and morphologies are assumed for different types of particles.

1. Pure, externally mixed black carbon aerosols are assumed to have a fractal aggregate morphology as shown in Fig. 1. The fractal morphology can be described by the statistical scaling law $N_s = k_0(R_g/a)^{D_f}$, where N_s denotes the number of spherical monomers in the aggregate, D_f and k_0 are the fractal dimension and fractal prefactor, a is the monomer radius, and $R_g = \sqrt{\sum_{n=1}^{N_s} r_n^2/N_s}$ is the radius of gyration, where r_n describes the distance of the nth monomer from the aggregate's centre of mass. We use $D_f = 1.8$, $k_0 = 1.3$, which is based on the review in Bond and Bergstrom (2006). Although in the atmosphere black carbon aggregates may also have higher fractal dimensions (e.g. Adachi et al., 2007), assuming a lower fractal dimension around 1.8 yields mass absorption cross sections that lie closer to experimental data, as was shown in Kahnert and Devasthale (2011). The monomer radius was assumed to be $a = 25$ nm. This is consistent with field observations (Adachi and Buseck, 2008); also, it was shown (Kahnert, 2010b) that this choice of monomer radius in light scattering computations yields results for the single-scattering albedo of black carbon aggregates consistent with observations.

   The calculation in Kahnert and Devasthale (2011) were limited to aggregates up to $N_s = 600$. In order to cover the size range of externally mixed black carbon in SALSA we had to extend these calculations to aggregate sizes up to $N_s = 2744$, which corresponds to a volume-equivalent radius of $R_V = 350$ nm (compare with Table 2). We used the multiple-sphere T-matrix code (Mackowski and Mishchenko, 2011), which is based on the numerically exact superposition T-matrix method for solving Maxwell's equations. Figure 2 shows some of the computed black car-

GMDD
8, 10735–10781, 2015

bon optical properties as a function of particle size and wavelength. All optical properties are averaged over particle orientations. The absorption cross section C_{abs} shows the characteristic decline $\sim 1/\lambda$ at long wavelengths, where the refractive index of black carbon is changing only slowly (Chang and Charalampopoulos, 1990). Also, C_{abs} increases with particle size. For small particle sizes this increase goes as $\sim R_V^3$, which is typical for the Rayleigh scattering regime (Mishchenko et al., 2002).

2. Black carbon aerosols that are internally mixed with other aerosol components are morphologically very complex. It is technically beyond the reach of our present capabilities to build an aerosol optics database with the use of morphologically realistic model particles. However, it is possible to employ realistic model particles in reference computations for some selected cases. This has recently been done in Kahnert et al. (2013). In that study, optical properties of encapsulated aggregate model particles, such as the one shown in Fig. 3 (left), were computed in the size range from 100–500 nm, for different black carbon volume fractions, and for wavelengths from the UV-C to the mid-IR. The morphological parameters characterising these model particles were based on field observations (Adachi and Buseck, 2008); the coating material was sulphate. The computations were performed with the discrete dipole approximation (Yurkin and Hoekstra, 2007).

   In Kahnert et al. (2013) the computational results were compared to those obtained with simple model particles, such as externally mixed homogeneous spheres, internally mixed homogeneous spheres, and concentric core-shell particles with a carbon core and a sulphate shell. The analysis revealed which morphological properties of the encapsulated aggregate particles had the dominant impact on the optical properties. There are two important properties: (1) the amount of carbon mass that interacts with the electromagnetic field has a major impact on the absorption cross section C_{abs}. In a core-shell model as well as in a model based on externally mixed homogeneous spheres, all of the black carbon is con-

GMDD
8, 10735–10781, 2015

centrated in a single sphere. Owing to absorption the electromagnetic field does not penetrate deeply into this sphere. Hence much of the carbon mass is shielded from interacting with the field, resulting in an underestimation of C_{abs} compared to the encapsulated aggregates, in which a much larger fraction of the carbon mass can contribute to the absorption of electromagnetic energy. By contrast, in a homogeneous internal mixture model the black carbon is distributed evenly throughout the sulphate host, which allows too much of the carbon mass to interact with the field. This results in an overestimation of C_{abs}. (2) Compared to a bare black carbon aggregate, a coated aggregate has a larger geometric cross section. Hence more light is intercepted by an internally mixed particle and focused onto the black carbon inclusion, thus enhancing C_{abs}. This effect is neglected in the external mixture model, resulting in an underestimation of C_{abs}.

Once we understand which morphological properties are most essential, and which ones make a minor contribution to the optical properties, we can devise model particles that account for the most important morphological effects, yet are sufficiently simple for computing a look-up table for large-scale modelling. It was proposed in Kahnert et al. (2013) to use a core-shell model (hence accounting for the coating effect) in which only part of the carbon mass is contained in the core, and the remaining part is homogeneously mixed with the shell. The model particle is illustrated in Fig. 3 (right). The core-shell partitioning of the carbon mass is a free parameter, with which one can interpolate between the two extreme models of the homogeneous mixture (all carbon mass mixed with the shell) and the regular core-shell model (all carbon mass in the core). This model has been referred to as the concentric core-grey-shell (CGS) model. The tuning of the free parameter in the model was done to fit the reference model of encapsulated aggregates as described in Kahnert et al. (2013). The CGS model has been employed in generating the new MATCH-optics look-up table. The shell material can be any mixture of water-soluble components. In the mass transport model, we assume that all SIA components and all sea salt is internally mixed. We further assume that in

GMDD
8, 10735–10781, 2015

size classes 1–4, 0, 70, 70, and 100 %, respectively, of the black carbon, 0, 70, 70, and 70 % of the organic carbon, and 0, 1.3, 1.3, and 1.3 % of the dust are internally mixed; the remaining BC, OC, and dust mass is externally mixed. In SALSA, the mixing state depends on the size bin (see Table 2), and the mixing proportions are provided by the model results. In both the mass transport model and in MATCH-SALSA, the contribution to the effective refractive index of dust and black carbon is computed by the Maxwell–Garnett EMT Maxwell Garnett (1904), while for all other components we use the Bruggemann EMT (Bruggemann, 1935).

3. All other externally mixed particles not containing black carbon are assumed to be homogeneous spheres in the present version of the look-up table.

The look-up tables contain results for C_{ext}, C_{sca}, g, and C_{bak} in 28 wavelength bands from the UV-C to the mid-IR. Computations with the CGS model were performed for 37 discrete BC volume fractions. For the shell material, as well as for non-carbon containing particles, the table contains (depending on the wavelength band) up to 40 discrete values of the real part and up to 18 discrete values of the imaginary part of the refractive index. The range of the refractive indices varies with wavelength; it is determined by those chemical components that, at each given wavelength, have the most extreme values of the refractive index. The optical properties are pre-averaged over particle sizes for each size bin. Thus we generated one look-up table each for the mass transport model with its four size bins, and for SALSA with its 20 size bins. It is assumed that the number density is constant in each size bin.

The MATCH-optics model computes in each grid cell and for each size bin the effective refractive index of the internally mixed material by use of EMT. The corresponding optical properties are obtained by interpolating the closest pre-computed results in the look-up table. Size-averaging is performed by weighing the optical cross sections as well as $g \cdot C_{sca}$ in each size bin with the number density per bin and adding over all bins. The integrated quantities are then divided by the total particle number density; the integral over $g \cdot C_{sca}$ is also divided by the size-averaged scattering cross section.

GMDD
8, 10735–10781, 2015

2.4 Evaluation of the optics models

The new internal-mixture optics model with its BC fractal aggregate and core-grey-shell model particles accounts for significant morphological details in aerosols. The main question we want to address is whether or not this high level of detail is really necessary, i.e., if it has any *significant* impact on optical properties modelled with a CTM. By *significant* we mean an impact that is comparable to other effects whose importance is well understood. Thus to make such an assessment we need to pick a well-understood effect that can serve as a gauge, i.e., to which we can compare the impact of particle morphology on optical properties. We take the effect of aerosol dynamics as a gauge. Thus we compute aerosol optical properties

1. with the MATCH mass-transport model (i.e., with aerosol dynamics switched off), in conjunction with the old optics model (abbreviated by MT-EXT, "mass-transport external mixture");

2. with the MATCH mass-transport model in conjunction with the new optics model (MT-CGS, "mass-transport core-grey-shell");

3. with the MATCH-SALSA model (i.e., with aerosol dynamics switched on), in conjunction with the new optics model (SALSA-CGS, "MATCH-SALSA core-grey-shell").

Comparison of 1. and 2. will allow us to assess the impact of the morphological assumptions in the aerosol optics model. Comparison of 2. and 3. will give us an estimate of how much the inclusion or omission of aerosol dynamic processes impacts modelling results of aerosol radiometric properties. As aerosol dynamics is well-known to have a substantial impact on aerosol concentrations and size distributions, this effect will provide us with a reference to which we can compare the impact of the morphological assumptions made in the aerosol optics model.

As an example, Fig. 4 shows the extinction aerosol optical depth (AOD) over the European model domain computed on 22 December 2007 at 12:00 UTC with MT-EXT

GMDD
8, 10735–10781, 2015

(left), MT-CGS (centre), and SALSA-CGS (right). The general spatial patterns are similar, as they should, since all three runs used the same EMEP emissions and HIRLAM meteorological data. However, the magnitude of the AOD results can differ significantly among the three model runs (note the semi-logarithmic scale!). Interestingly, differences between the two optics models (left and centre) are roughly on the same order as those between the mass-transport and aerosol dynamic models (centre and right).

Thus a first inspection of computed fields of aerosol optical properties suggests that the level of detail in the morphological assumptions of the aerosol optics model may be significant for the modelling results. In a next step we quantify differences in modelled aerosol radiative forcing among the three model versions. To this end we pick four geographic locations that are indicated by circles in Fig. 4; one site over Northern Italy (45.0° N, 8.5° E), one over the Mediterranean Sea (37.5° N, 5.5° E), one over Poland (52.6° N, 21.0° E), and one over the North Sea (52.0° N, 2.7° E). We further pick two instances representing low-BC summer and high-BC winter conditions, namely, 22 June 2007 12:00 UTC, and 22 December 2007 12:00 UTC. Radiative transfer calculations are performed for each of these four sites and for both instances. Vertical profiles of the aerosol optical depth per layer, the single-scattering albedo, and the asymmetry parameter are used as input to the libRadtran radiative transfer package (Kylling et al., 1998), assuming a plane-parallel atmosphere. For the surface albedo of the ocean we assume a spectrally constant value of 0.065, while for the spectrally varying surface albedo of the two land locations we used MODIS observations for each of the two instances. The results were spectrally integrated to obtain the broadband radiative fluxes. The radiative transfer simulations were repeated for corresponding profiles of optical properties in the absence of black carbon, as well as for clear-sky conditions. This allows us to compute differences in broadband radiative fluxes, i.e., the radiative effect of black carbon, and the radiative effect of all aerosols. The results of this radiative transfer study are discussed in Sect. 3.1.

To further investigate the significance of the optics model on radiometric properties, we look at remote sensing-related optical properties, namely, backscattering coefficient

GMDD
8, 10735–10781, 2015

and Ångström exponent. These results are discussed in Sects. 3.3 and 3.4, respectively.

3 Results

3.1 Optical properties and radiative forcing

The result for the optical properties obtained with the three model versions (AOD per layer, SSA and g) at the wavelength 532(CGS)/500(EXT) nm, together with the radiative forcing for aerosols and black carbon can be seen in Figs. 5–8 for Northern Italy and the Mediterranean on 22 June 2007. Each figure shows the differences in direct solar flux ΔF_s (top left), diffuse downwelling flux ΔF_d (top right), diffuse upwelling flux ΔF_u (centre left), and net radiative flux $\Delta F_{net} = \Delta F_s + \Delta F_d - \Delta F_u$ (centre right), where either the difference between aerosol-laden and clear sky conditions are considered (Figs. 5 and 6), or the difference between fluxes in the presence and absence of black carbon (Figs. 7 and 8). Top-of-atmosphere (TOA) results for the other geographical locations are summarized in terms of aerosol forcing in Table 3 and black carbon forcing in Table 4. The wavelengths 532(CGS)/500(EXT) nm are near the maximum of the solar spectrum. At other wavelengths (not shown) the optical properties behave similarly. Each figure has a vertical span of 6 km, which comprises that part of the troposphere where almost all aerosols are concentrated in the cases we picked.

Before starting our analysis, we note that the magnitude of the radiative fluxes generally depends on the concentration of aerosols. As we cannot claim that the test cases we happened to pick are in any way representative for *typical* aerosol and black carbon loads, we are not focusing on the *magnitude* of the radiative fluxes here. Rather, we want to compare the *differences* in radiative fluxes among the three model versions.

GMDD
8, 10735–10781, 2015

3.1.1 Comparison of aersol dynamics and mass-transport model

We start by comparing radiative fluxes in the presence and absence of aerosols, which we refer to as the "aerosol radiative effects". Figures 5 and 6 show the aerosol radiative effects modelled over Northern Italy and over the Mediterranean north of Algier, respectively. The general patterns in both plots can be understood as follows. In the presence of aerosols, optical extinction is stronger than in clean air. Thus the presence of aerosols gives a reduction ΔF_s of the direct solar flux (upper left). As the aerosol optical depth per atmospheric layer strongly increases near the ground, the magnitude of ΔF_s increases with decreasing altitude. Further, aerosol extinction results in the generation of diffuse flux; the downwelling diffuse flux accumulates downward, resulting in an increasing excess of downwelling flux ΔF_d in the presence of aerosols as one approaches the surface. The upwelling flux F_u is generated by scattering in the atmosphere and reflection at the surface. Since aerosol extinction reduces the total flux as one approaches the surface, less upwelling diffuse flux is generated at low altitudes; hence the difference in upwelling flux ΔF_u between an aerosol-laden and a clear sky atmosphere is negative near the surface. However, it increases with altitude, because at higher altitudes the difference (aerosol – clear sky) in the total flux that can be converted into upwelling diffuse flux decreases at higher altitudes.

If we focus now on differences in the radiative net flux ΔF_{net} at high altitudes, i.e., the radiative forcing effect of aerosols, then we see significant differences between the mass transport model (MT, red) and SALSA (green) at both geographic locations. It is evident that the main cause for these are corresponding differences in the diffuse upwelling flux ΔF_u.

At both locations the diffuse upwelling flux is smaller for SALSA then for MT, but for different reasons. Over the Mediterranean (Fig. 6), the AOD is significantly smaller for SALSA than for MT, resulting in less extinction of the direct flux, hence less generation of diffuse flux, and a smaller radiative cooling effect for SALSA.

GMDD
8, 10735–10781, 2015

Over Northern Italy (Fig. 5), there is almost no difference in AOD between the two models. It can be seen from the AOD profile that the majority of aerosols reside in the lowest 1 km near the surface. However, above 1 km the results of ΔF_u obtained with SALSA and MT diverge with increasing altitude. This is a result of the reflection by the near-surface aerosol layer, which is slightly different in the two models. In MT the SSA is higher than in SALSA, resulting in more scattering, thus in more diffuse radiation. The asymmetry parameter is slightly larger in MT than in SALSA; correspondingly, the partitioning in MT between downwelling and upwelling radiation is somewhat shifted in favour of the former. However, this only partially counteracts the generation of a higher amount of diffuse upwelling radiation in MT due to the higher SSA. The net effect is a higher value of ΔF_u in MT, hence a larger radiative cooling effect at higher altitudes.

To further analyse the difference in optical properties between MT and SALSA, we look at the aerosol masses and the relative sizes of the particles. Figure 9 shows vertical profiles of the effective radius of the size distributions in SALSA (green) and the MT model (black) over Northern Italy (left) and over the Mediterranean (right). Figure 10 shows profiles for the total aerosol mass (1st row), BC (black carbon) (2nd row), sulphate (3rd row), and nitrate (4th row) for both Northern Italy (1st column) and Mediterranean (2nd column). We focus on the total aerosol mass, which is expected to impact the aerosol optical depth. The aerosol optical depth is dependent on the number density (which, in turn, increases with the mass mixing ratio), as well as on the extinction cross section (which generally increases with the effective radius of the particles). Over Northern Italy, the SALSA model predicts a larger mass mixing ratio than the MT model (Fig. 10, upper left), but also a smaller particle size (Fig. 9, left). These two effects cancel almost exactly, resulting in nearly identical aerosol optical depths predicted with the two models (Fig. 5, bottom left). By contrast, over the Mediterranean the two models predict similar mass mixing ratios (Fig. 10, upper right), while SALSA predicts a much lower effective radius than the MT model (Fig. 9, right). As a consequence, the optical depth is significantly lower in SALSA than in MT (Fig. 6, bottom left). The SSA is

GMDD
8, 10735–10781, 2015

lower in SALSA than in MT. This is mainly caused by the fact that the effective radius is smaller in SALSA than in MT, since SSA is usually increasing with size.

The radiative impacts summarised in Table 3 show the same behaviour as Figs. 5 and 6 at three of the four geographical locations. The Polish site deviates, since SALSA produces a much larger radiative cooling than the MT model. This can be explained by SALSA having a larger amount of aerosols throughout the column at that site, especially more sulphate, which, when externally mixed, contributes to a larger amount of scattering and therefore a higher SSA and a larger diffuse upwelling radiative flux.

We now compare radiative fluxes in the presence and absence of black carbon, which we refer to as the "black carbon radiative effect". Figures 7 and 8 show the radiative effect of black carbon together with the optical properties with and without black carbon. Again, the dominant feature of ΔF_{net} at TOA comes from corresponding differences in the upwelling diffuse radiative flux ΔF_{u}. In these figures, we have to focus on the difference in the optical properties when analysing the radiative fluxes. The general pattern can be seen in Fig. 7, which shows the differences in radiative fluxes and in the optical properties over Northern Italy. The direct solar flux (upper left) decreases with decreasing altitude owing to extinction. The magnitude of the decrease mainly reflects the differences in optical depth in the presence and absence of black carbon (bottom left), which is slightly larger in SALSA than in MT. The decrease in solar flux does not automatically result in an increase in the downwelling diffuse flux with decreasing altitude (upper right), as it was in the comparison of fluxes in the presence and absence of *all* aerosols. The situation is more complex now. Near the surface, where the optical depth is largest, the difference in SSA in the presence and absence of black carbon is quite large in the MT model (bottom centre, red lines), and slightly smaller in SALSA (green lines). As a result, absorption contributes more to the total extinction in the MT model than in SALSA (at least near the surface). Hence, the portion of the downwelling flux that is absorbed on its way downward is larger in the MT model than in SALSA, resulting in a decrease of the diffuse downwelling flux with decreasing altitude (upper right, red line). The differences between the two models in the diffuse upwelling flux

GMDD
8, 10735–10781, 2015

are very small (centre left, red and green lines). This is the result of cancelling effects; for instance, there is less direct solar flux, but more diffuse downwelling flux in SALSA that can be converted into diffuse upwelling flux through scattering. As a result, the differences between both models in the net flux (centre right, red and green lines) are almost negligible.

Figure 8 shows the radiative effect of black carbon over the Mediterranean. Again, the dominant feature of ΔF_{net} at TOA comes from corresponding differences in the upwelling diffuse radiative flux ΔF_u. The difference between MT and SALSA are not as prominent here, mainly due to the fact that the differences in the optical properties are similar, especially in the SSA. There is still a small difference for the Mediterranean, where SALSA has a larger radiative cooling than MT. This difference is very small, but it may come from the slight difference in the AOD combined with the difference in SSA from above 1 km, where SALSA has a marginally larger difference than MT, creating the difference in the net radiative flux above 1 km. Another possibility is that these small differences are caused by multiple scattering effects, which are notoriously difficult to understand by an intuitive approach. If studying the differences in AOD and SSA for the twelve wavelengths used in this study (not shown), the differences for SALSA AOD and SSA are smaller for the long-wave (LW) part of the spectrum (533.2–3461.5 nm). This results in less LW extinction and scattering and slightly more radiative cooling for SALSA.

Table 4 shows the black carbon forcing for all the four geographical locations and both months. In June the difference at the TOA is very small between MT and SALSA for all the locations, but larger for the Mediterranean as noted in Fig. 8. The month of December shows a pattern where SALSA has a higher radiative heating over land, and smaller over the ocean compared to MT. This is strongly coupled to the larger difference in BC amounts over land than over the oceans, where the two models have similar values all through the column, see Fig. 10 for Northern Italy and Mediterranean. Poland and North Sea are not shown here, but show similar behaviour.

GMDD
8, 10735–10781, 2015

3.1.2 Comparison of the two optics models

The comparison between SALSA and the MT model in the previous section served two purposes. First, it helped us to develop a basic understanding for the effects of aerosols and black carbon on radiative fluxes. Second, it provided us with a gauge for assessing the importance of the aerosol optics model, which will be the subject of this section.

We compare the old EXT (blue line) and the new CGS (red line) optics models in Figs. 5 and 6, each used in conjunction with the MT-version of MATCH. The net radiative flux ΔF_{net} in the CGS model shows a weaker TOA cooling effect than the EXT model, both over Northern Italy and over the Mediterranean. Again, the upwelling flux has the dominant impact on the behaviour of the TOA net radiative flux. Over Northern Italy (Fig. 5) the diffuse upwelling flux is larger for the EXT model above 1 km, whereas it is smaller below 1 km and at the bottom of the atmosphere (BOA). The AOD profile reveals that in the EXT model extinction is stronger than in the CGS model throughout the tropospheric column. As a result, there is more diffuse downwelling flux being generated in EXT than in CGS. At the bottom of the atmosphere (BOA) extinction of the direct flux is stronger than generation of diffuse downwelling flux; hence less downwelling flux is reflected by the surface, resulting in less BOA upwelling diffuse flux in EXT than in CGS. Higher up in the troposphere, the upwelling diffuse flux is mostly generated by atmospheric scattering rather than reflection from the surface. As the SSA in EXT is higher than in CGS, more diffuse flux is generated, resulting in a stronger radiative cooling effect in EXT than in CGS.

Over the Mediterranean (Fig. 6), the EXT and CGS model have almost identical AOD profiles in the green part of the spectrum. However, at longer wavelengths (not shown) EXT predicts substantially higher AOD values than CGS. This explains the larger amount of diffuse broadband radiation generated in the EXT model, which results in a stronger negative TOA net flux in EXT as compared to the CGS model. Note that the differences in SSA between EXT and CGS are fairly small, while the differences in g are rather large. The higher values of g in EXT may contribute to the large amount

GMDD
8, 10735–10781, 2015

of diffuse downdwelling radiation in that model; however, the dominant effect is likely to be the high optical depth at red and IR wavelengths.

Table 3 summarises the TOA net radiative flux at all four geographical locations for both June and December. The largest differences among the models are seen in December at the two northernmost locations, i.e., Poland and the North Sea. At these two places, the total aerosol amount (not shown) is significantly higher than at the other two locations farther south, giving rise to a larger absolute changes in the aerosol forcing.

The black carbon forcing looks rather different at the two geographical locations. Over Northern Italy, the black carbon forcing is more significant due to higher levels of BC, see Fig. 10. As can be seen in Fig. 7, the differences in optical properties computed with and without black carbon are larger in the CGS model than in the EXT model, particularly for the SSA. This means that in the CGS model the presence of black carbon causes more absorption than in the EXT model, thus generating less diffuse down- and upwelling flux by scattering. As a result, the CGS model predicts more radiative warming, i.e., a higher TOA radiative net flux than the EXT model. The reason for this is that (i) the CGS model treats externally mixed soot as aggregates, which have a lower SSA than the massive black carbon spheres in the EXT model; and (ii) the CGS model treats internally mixed soot as a coated core-grey-shell model, which accounts for focusing of electromagnetic radiation onto the carbon core, thus enhancing absorption, i.e., lowering the SSA, while the EXT model treats *all* black carbon as externally mixed.

3.2 Gauging the significance of aerosol optics modelling

Now that we have understood the impact of the aerosol optical properties on radiative fluxes, we finally turn to the main question of this study. We ask if the level of detail in aerosol optics modelling has a significant impact on observable radiometric properties. As a gauge we consider the changes in radiometric properties caused by the inclusion or omission of aerosol dynamic processes. Thus we compare in Figs. 5–8 the differences in radiative forcing between the red and green lines to the corresponding

GMDD
8, 10735–10781, 2015

differences in the red and blue lines. We see that in some cases the choice of optics model has a stronger effect than the inclusion of aerosol dynamics (e.g. Fig. 7), while in other cases it is the other way round (e.g. Fig. 6). We can also inspect Tables 3 and 4 and arrive at the same result. On average, the effect of including aerosol dynamics on the TOA radiative forcing is of comparable magnitude as the effect caused by employing a more realistic aerosol optics model. In the following two subsections, we will discuss the significance of the optics model for radiometric quantities that are relevant for remote sensing applications.

3.3 Backscattering coefficient

From ground-based and space-borne lidars measurements one can obtain the aerosol backscattering coefficient β, which is proportional to the backscattering cross section C_{bak} of the particles and the aerosol number density. Figure 11 shows vertical profiles of β computed at two locations and at two instances, as indicated in the figure headings. Each panel shows computational results obtained with the three different model versions. The figure shows results for the second Nd:YAG harmonic of 532 nm. Corresponding results computed for wavelengths of 355 and 1064 nm lead to similar conclusions.

We saw in Fig. 10 for June over Northern Italy (upper left) that SALSA predicts an aerosol mass mixing ratio, hence a particle number density, that is higher than that in the MT model. But we also saw in Fig. 9 (left) that SALSA predicts lower values of r_{eff}. This results in lower values of C_{bak}. We see in Fig. 11 (upper left) that the effect on β of the higher number density dominates over the effect of the lower r_{eff}, resulting in values of β that are about 30 % higher in SALSA (green line) than in the MT model (red line). Over the Mediterranean, both SALSA and the MT model predict similar mass densities (Fig. 10, upper right); but SALSA still predicts substantially lower values of r_{eff} (Fig. 9, right). The result is that β computed with the MT model (red line) is almost twice as high as the corresponding results obtained with SALSA (green line) (Fig. 11, upper right).

GMDD
8, 10735–10781, 2015

A similar comparison of the two optics models (red and blue lines in Fig. 11) shows that the new CGS optics model consistently predicts substantially lower values of β than the old EXT optics model. This agrees with the comparison shown in Kahnert et al. (2013) between encapsulated black carbon aggregates and externally mixed homogeneous spheres. (In a retrieval algorithm, an optics model that overestimates the backscattering cross section would result in underestimated retrieval results for the particle number density.) The differences between the two optics models are on the same order of magnitude (and often even slightly larger) than the corresponding differences between the SALSA and the MT versions of the aerosol transport model.

3.4 Ångström exponent

The Ångström exponent α in a wavelength interval $[\lambda_1, \lambda_2]$ is defined as

$$\alpha = -\frac{\log(\tau(\lambda_1)/\tau(\lambda_2))}{\log(\lambda_1/\lambda_2)}, \quad (1)$$

where τ denotes the extinction optical depth. This quantity is often used for obtaining particle size information (usually, the smaller the particle size, the larger α). Table 5 shows values of α for our different test cases computed with the three model versions in the wavelength interval 532–1064 nm. If we compare the columns labelled MT-CGS and SALSA-CGS, then we see that the mass-transport model consistently gives lower values of α. This is related to the high values of r_{eff} in that model, which we noted earlier. On the other hand, if we compare the columns labelled MT-EXT and MT-CGS, then we see that the new optics model (CGS) predicts higher values of α than the old model (EXT) in the first six rows, and lower values in the last two rows. This indicates that the errors introduced by the simple external-mixture model in computing α are quite unpredictable, even the sign of the error. When used in a size retrieval algorithm the retrieval errors caused by the EXT model would be equally hard to predict. The difference between the MT and SALSA model is somewhat larger, but not much larger,

GMDD
8, 10735–10781, 2015

than the differences between the old and new optics models. Note that the performance of the MT model could be improved in comparison to SALSA by modifying the assumed size distribution in the MT model. By contrast, the differences between the two optics models is rather fundamental; it is caused by the over-simplified treatment of aerosol morphology in the EXT model.

4 Conclusions

We have implemented a new aerosol optics model in a regional chemical transport model. The new model differs from an earlier optics model described in Kahnert (2008) in three essential points. (i) While the old model treats all chemical components as externally mixed, the new model accommodates both external and internal mixtures of aerosol species. (ii) The old model treats black carbon aerosols as homogeneous spheres; the new model assumes a fractal aggregate morphology with fractal parameters based on observations. Mass absorption cross sections and single scattering albedos computed with this model have previously been evaluated by comparison with measurements (Kahnert, 2010b). (iii) The new model describes internally mixed black carbon aerosols by a recently developed "core-grey-shell" model (Kahnert et al., 2013). This model accounts for the inhomogeneous internal mixing state of black carbon aggregates encapsulated in a shell of liquid-phase material. The model has been evaluated by comparison with reference computations based on observation-derived realistic models for encapsulated fractal aggregates (Kahnert et al., 2013). Item (i) has been incorporated in other CTMs earlier (e.g. Saide et al., 2013); however, to the best of our knowledge, items (ii) and (iii) go significantly beyond the current state-of-the-art of aerosol optics models employed in CTMs. The main question of the present study is whether or not such a substantial level of detail in the description of aerosol morphology and optical properties is needed in a CTM.

To this end we compare radiative fluxes, backscattering coefficients, and Ångström exponents modelled with the old and new optics models. To gauge the differences

GMDD
8, 10735–10781, 2015

we observe, we further compare two model versions of the CTM with different levels of detail in the aerosol process descriptions, namely, one version that includes aerosol dynamic processes, and one simpler mass-transport model, in which aerosol dynamics is switched off. The importance of aerosol dynamics is well understood an can therefore serve as a reference. The comparison showed that both for radiative fluxes, and for backscattering coefficients, and for Ångström exponents the differences between the two different optics models are of similar magnitude as corresponding differences between an aerosol dynamics and a mass-transport model. This strongly suggests that over-simplified aerosol optics models are likely to introduce substantial errors in modelled radiative fluxes and remote sensing-relevant observables. In Earth-system models such errors would enter into the simulation of the direct aerosol radiative forcing effect and add to all other sources of error in the model. In model evaluations that make use of remote sensing observations these errors would complicate the comparison between model results and observations.

The modifications to the optics model studied here were limited to black carbon aerosols. There are many other aerosols with complex morphological properties, such as mineral dust, which our optics model still treats by an over-simplified homogeneous sphere model. The findings of our study should be an incentive for improving the description of dust and volcanic ash optical modelling in CTMs. A review of our current state of knowledge on aerosol morphology and aerosol optics for a variety of different aerosols has recently been reviewed in Kahnert et al. (2014).

The findings of this study are likely to have implications for chemical data assimilation. In data assimilation one employs an *observation operator* that maps the model results to observable quantities. In case of satellite-based observations of aerosol optical properties, the observation operator is just our aerosol optics model, possibly coupled to a radiative transfer model. Many data assimilation methodologies, such as the variational method, require a linear (or, at least, linearised) observation operator. In the old optics model, which assumes externally mixed aerosols, the observation operator is, indeed, linear (Kahnert, 2008). This largely explains why external-mixture optics models

GMDD
8, 10735–10781, 2015

are widely used in chemical data assimilation systems (e.g. Kahnert, 2008; Benedetti et al., 2009; Liu et al., 2011). However, the new optics model we introduced here does not provide us with a linear map from the aerosol concentrations to the optical parameters. To what extend one could linearise this model and make use of its Jacobian in a data assimilation system mainly depends on the degree of nonlinearity, which would need to be investigated thoroughly.

All datasets used in this study, the MATCH model data and the aerosol optics data are available upon request contacting the second author.

Acknowledgements. E. Andersson acknowledge funding from the Swedish National Space Board within the OSCES project (No. 101/13). M. Kahnert has been funded by the Swedish Research Council (Vetenskapsrådet) within the AGES project (project 621-2011-3346).

References

Adachi, K. and Buseck, P. R.: Internally mixed soot, sulfates, and organic matter in aerosol particles from Mexico City, Atmos. Chem. Phys., 8, 6469–6481, doi:10.5194/acp-8-6469-2008, 2008. 10737, 10745, 10746

Adachi, K., Chung, S. H., Friedrich, H., and Buseck, P. R.: Fractal parameters of individual soot particles determined using electron tomography: Implications for optical properties, J. Geophys. Res., 112, D14202, doi:10.1029/2006JD008296, 2007. 10745

Andersson, C., Langner, J., and Bergström, R.: Interannual variation and trends in air pollution over Europe due to climate variability during 1958–2001 simulated with a regional CTM coupled to the ERA40 reanalysis, Tellus B, 59, 77–98, 2007. 10740, 10741

Andersson, C., Bergström, R., Bennet, C., Robertson, L., Thomas, M., Korhonen, H., Lehtinen, K. E. J., and Kokkola, H.: MATCH-SALSA – Multi-scale Atmospheric Transport and CHemistry model coupled to the SALSA aerosol microphysics model – Part 1: Model description and evaluation, Geosci. Model Dev., 8, 171–189, doi:10.5194/gmd-8-171-2015, 2015. 10742

Benedetti, A., Morcrette, M. J.-J., Boucher, O., Dethof, A., Engelen, R. J., Huneeus, M. F. H. F. N., Jones, L., and S. Kinne, J. W. K., Mangold, A., Razinger, M., Simmons, A. J., and Suttie, M.: Aerosol analysis and forecast in the European Centre for

GMDD
8, 10735–10781, 2015

Medium-Range Weather Forecasts Integrated Forecast System: 2. Data assimilation, J. Geophys. Res., 114, D13205, doi:10.1029/2008JD011115, 2009. 10738, 10743, 10762
Bond, T. C. and Bergstrom, R. W.: Light absorption by carbonaceous particles: An investigative review, Aerosol Sci. Tech., 40, 27–67, 2006. 10745
Bruggemann, D. A. G.: Berechnung verschiedener physikalischer Konstanten von heterogenen Substanzen. 1. Dielektrizitätskonstanten und Leitfähigkeiten der Mischkörper aus isotropen Substanzen, Ann. Phys.-Berlin, 24, 636–664, 1935. 10744, 10748
Chang, H. and Charalampopoulos, T. T.: Determination of the wavelength dependence of refractive indices of flame soot, P. R. Soc. A, 430, 577–591, 1990. 10746
Dubovik, O., Sinyuk, A., Lapyonok, T., Holben, B. N., Mishchenko, M. I., Yang, P., Eck, T. F., Volten, H., Muñoz, O., Veihelmann, B., van der Zande, W. J., Leon, J.-F., Sorokin, M., and Slutsker, I.: Application of spheroid models to account for aerosol particle nonsphericity in remote sensing of desert dust, J. Geophys. Res., 111, D11208, doi:10.1029/2005JD006619, 2006. 10738
Foltescu, V., Pryor, S. C., and Bennet, C.: Sea salt generation, dispersion and removal on the regional scale, Atmos. Environ., 39, 2123–2133, 2005. 10741
Gerber, H. E.: Relative-humidity parameterization of the Navy Aerosol Model (NAM), Tech. Rep. 8956, Naval Research Laboratory, Washington, DC, 1985. 10744
Jones, A. R.: Light scattering in combustion, in: Light Scattering Reviews, edited by: Kokhanovsky, A., Springer, Berlin, 393–444, 2006. 10737
Kahnert, F. M.: Reproducing the optical properties of fine desert dust aerosols using ensembles of simple model particles, J. Quant. Spectrosc. Ra., 85, 231–249, 2004. 10738
Kahnert, M.: Variational data analysis of aerosol species in a regional CTM: background error covariance constraint and aerosol optical observation operators, Tellus B, 60, 753–770, 2008. 10738, 10743, 10744, 10760, 10761, 10762
Kahnert, M.: Modelling the optical and radiative properties of freshly emitted light absorbing carbon within an atmospheric chemical transport model, Atmos. Chem. Phys., 10, 1403–1416, doi:10.5194/acp-10-1403-2010, 2010a. 10739, 10743
Kahnert, M.: On the discrepancy between modelled and measured mass absorption cross sections of light absorbing carbon aerosols, Aerosol Sci. Tech., 44, 453–460, 2010b. 10745, 10760

GMDD
8, 10735–10781, 2015

Kahnert, M. and Devasthale, A.: Black carbon fractal morphology and short-wave radiative impact: a modelling study, Atmos. Chem. Phys., 11, 11745–11759, doi:10.5194/acp-11-11745-2011, 2011. 10745

Kahnert, M., Nousainen, T., and Lindqvist, H.: Models for integrated and differential scattering optical properties of encapsulated light absorbing carbon aggregates, Opt. Express, 21, 7974–7993, 2013. 10739, 10746, 10747, 10759, 10760

Kahnert, M., Nousiainen, T., and Lindqvist, H.: Review: Model particles in atmospheric optics, J. Quant. Spectrosc. Ra., 146, 41–58, 2014. 10738, 10761

Kokkola, H., Korhonen, H., Lehtinen, K. E. J., Makkonen, R., Asmi, A., Järvenoja, S., Anttila, T., Partanen, A.-I., Kulmala, M., Järvinen, H., Laaksonen, A., and Kerminen, V.-M.: SALSA – a Sectional Aerosol module for Large Scale Applications, Atmos. Chem. Phys., 8, 2469–2483, doi:10.5194/acp-8-2469-2008, 2008. 10742

Kupiainen, K. and Klimont, Z.: Primary emissions of submicron and carbonaceaous particles in Europe and the potential for their control, Tech. Rep. IR-04-079, IIASA, Laxenburg, Austria, 2004. 10741

Kupiainen, K. and Klimont, Z.: Primary emissions of fine carbonaceous particles in Europe, Atmos. Environ., 41, 2156–2170, 2007. 10741

Kylling, A., Bais, A. F., Blumthaler, M., Schreder, J., Zerefos, C. S., and Kosmidis, E.: The effect of aerosols on solar UV irradiances during the photochemical activity and solar ultraviolet radiation campaign, J. Geophys. Res., 103, 26051–26060, 1998. 10750

Liu, Z., Liu, Q., Lin, H.-C., Schwartz, C. S., Lee, Y.-H., and Wang, T.: Three-dimensional variational assimilation of MODIS aerosol optical depth: Implementation and application to a dust storm over East Asia, J. Geophys. Res., 116, D23206, doi:10.1029/2011JD016159, 2011. 10762

Mackowski, D. W. and Mishchenko, M. I.: A multiple sphere T-matrix Fortran code for use on parallel computer clusters, J. Quant. Spectrosc. Ra., 112, 2182–2192, 2011. 10745

Mårtensson, E. M., Nilsson, E. D., de Leeuw, G., Cohen, L. H., and Hansson, H.-C.: Laboratory simulations and parameterization of the primary marine aerosol production, J. Geophys. Res., 108, 4297, doi:10.1029/2002JD002263, 2003. 10741

Maxwell Garnett, J. C.: Colours in metal glasses and in metallic films, Philos. T. R. Soc. A, 203, 385–420, 1904. 10748

Mishchenko, M. I., Travis, L. D., and Lacis, A. A.: Scattering, Absorption, and Emission of Light by Small Particles, Cambridge University Press, Cambridge, 2002. 10746

GMDD
8, 10735–10781, 2015

Monahan, E. C., Spiel, D. E., and Davidson, K. L.: A model of marine aerosol generation via whitecaps and wave disruption, in: Oceanic Whitecaps and their Role in Air-Sea Exchange, edited by: Monahan, E. C. and Niocaill, G. M., D Reidel, Norwell, MA, 167–174, 1986. 10741

Neusüß, C., Wex, H., Birmili, W., Wiedensohler, A., Koziar, C., Busch, B., Brüggemann, E., Gnauk, T., Ebert, M., and Covert, D. S.: Characterization and parameterization of atmospheric particle number-, mass-, and chemical-size distributions in central Europe during LACE 98 and MINT, J. Geophys. Res., 107, LAC 9-1–LAC 9-13, doi:10.1029/2001JD000514, 2002. 10744

Nousiainen, T.: Optical modeling of mineral dust particles: a review, J. Quant. Spectrosc. Ra., 110, 1261–1279, 2009. 10737

Nousiainen, T., Kahnert, M., and Veihelmann, B.: Light scattering modeling of small feldspar aerosol particles using polyhedral prisms and spheroids, J. Quant. Spectrosc. Ra., 101, 471–487, 2006. 10738

Robertson, L., Langner, J., and Engardt, M.: An Eulerian limited-area atmospheric transport model, J. Appl. Meteorol., 38, 190–210, 1999. 10741

Saide, P. E., Carmichael, G. R., Liu, Z., Schwartz, C. S., Lin, H. C., da Silva, A. M., and Hyer, E.: Aerosol optical depth assimilation for a size-resolved sectional model: impacts of observationally constrained, multi-wavelength and fine mode retrievals on regional scale analyses and forecasts, Atmos. Chem. Phys., 13, 10425–10444, doi:10.5194/acp-13-10425-2013, 2013. 10738, 10760

Yurkin, M. A. and Hoekstra, A. G.: The discrete dipole approximation: an overview and recent developments, J. Quant. Spectrosc. Ra., 106, 558–589, 2007. 10746

GMDD
8, 10735–10781, 2015

Table 1. Size bins (characterised by the radius r) and chemical species in the MATCH mass transport model. The labels "p" and "s" refer to primary emitted particles and secondary particles generated from gas precursors.

size bin	r (nm)	OC	BC	wind blown	other PPM	NaCl	$(NH_4)_2SO_4$	NH_4NO_3	other PSO_x	other PNO_x
1	10–50	p	p		p	p	s	s	s	s
2	50–500	p	p		p	p	s	s	s	s
3	500–1250					p	s	s	s	s
4	1250–5000	p	p	p	p	p	s	s	s	s

GMDD
8, 10735–10781, 2015

Table 2. Size bins and chemical species in the MATCH-SALSA aerosol dynamic transport model. An "x" marks that the species is present in a particular size bin.

size bin	r (nm)	mixing state	OC	BC	other PPM	NaCl	PSO_x	PNO_x	PNH_x
1	1.5–3.8	internal	x				x		x
2	3.8–9.8	internal	x				x		x
3	9.8–25	internal	x				x		x
4	25–49	internal+H_2O	x	x	x	x	x		x
5	49–96	internal+H_2O	x	x	x	x	x		x
6	96–187	internal+H_2O	x	x	x	x	x		x
7	187–350	internal+H_2O	x	x	x	x	x		x
8	25–49	external	x	x			x		x
9	49–96	external	x	x			x		x
10	96–187	external	x	x			x		x
11	187–350	external	x	x	x		x		x
12	350–873	NaCl+H_2O				x			
13	873–2090	NaCl+H_2O				x			
14	2090–5000	NaCl+H_2O				x			
15	350–873	internal+H_2O	x	x	x		x	x	x
16	873–2090	internal+H_2O	x		x		x		x
17	2090–5000	internal+H_2O	x		x		x		x
18	350–873	internal+H_2O			x		x		x
19	873–2090	internal+H_2O			x		x		x
20	2090–5000	internal+H_2O			x		x		x

GMDD
8, 10735–10781, 2015

Table 3. The aerosol forcing at the top of the atmosphere (TOA), $\Delta F_{\text{net,TOA}}$ [W m^{-2}], for the four different geographical locations, one summer and one winter event, and three model versions.

		MT-EXT	MT-CGS	SALSA-CGS
Summer	Poland	−0.21	−0.21	−0.77
	North Sea	−0.34	−0.29	−0.24
	Northern Italy	−0.06	−0.05	0.01
	Mediterranean	−1.20	−0.99	−0.30
Winter	Polen	−4.41	−2.00	−2.18
	North Sea	−2.85	−1.21	−0.86
	Northern Italy	−1.15	−0.53	−0.57
	Mediterranean	−0.09	−0.04	−0.03

GMDD
8, 10735–10781, 2015

Table 4. The black carbon forcing at the top of the atmosphere (TOA), $\Delta F_{\text{net,TOA}}$ [W m^{-2}], for the four different geographical locations, one summer and one winter event, and three model versions.

		MT-EXT	MT-CGS	SALSA-CGS
Summer	Poland	1.02×10^{-2}	1.16×10^{-2}	1.20×10^{-2}
	North Sea	1.71×10^{-2}	1.54×10^{-2}	1.49×10^{-2}
	Northern Italy	4.61×10^{-2}	7.77×10^{-2}	7.86×10^{-2}
	Mediterranean	8.54×10^{-3}	6.45×10^{-3}	2.41×10^{-3}
Winter	Poland	4.03×10^{-2}	3.56×10^{-2}	6.83×10^{-2}
	North Sea	1.95×10^{-2}	2.28×10^{-2}	4.97×10^{-3}
	Northern Italy	6.73×10^{-2}	1.08×10^{-1}	1.46×10^{-1}
	Mediterranean	6.03×10^{-4}	1.34×10^{-3}	3.13×10^{-4}

GMDD
8, 10735–10781, 2015

Table 5. Ångström exponent in the wavelength region 532–1064 nm for the four different geographical locations, one summer and one winter event, and three model versions.

		MT-EXT	MT-CGS	SALSA-CGS
Summer	Poland	0.32×10^{0}	0.12×10^{1}	0.28×10^{1}
	North Sea	0.80×10^{0}	0.12×10^{1}	0.21×10^{1}
	Northern Italy	0.11×10^{1}	0.11×10^{1}	0.15×10^{1}
	Mediterranean	0.36×10^{0}	0.12×10^{1}	0.21×10^{1}
Winter	Poland	0.80×10^{0}	0.12×10^{1}	0.22×10^{1}
	North Sea	0.79×10^{0}	0.11×10^{1}	0.14×10^{1}
	Northern Italy	0.13×10^{1}	0.10×10^{1}	0.12×10^{1}
	Mediterranean	0.13×10^{1}	0.98×10^{0}	0.14×10^{1}

GMDD
8, 10735–10781, 2015

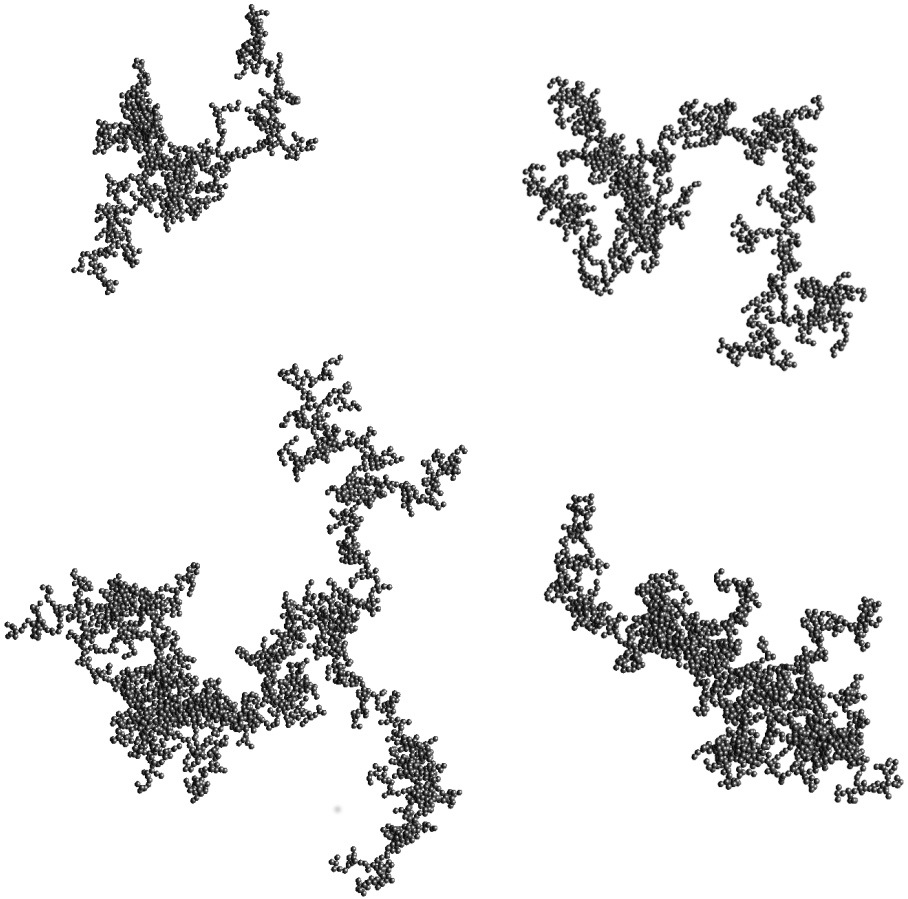

Figure 1. Examples of fractal aggregate model particles for computing optical properties of externally mixed black carbon. The aggregates consist of 1000, 1500, 2000, and 2744 monomers (in clockwise order, starting from upper left).

GMDD
8, 10735–10781, 2015

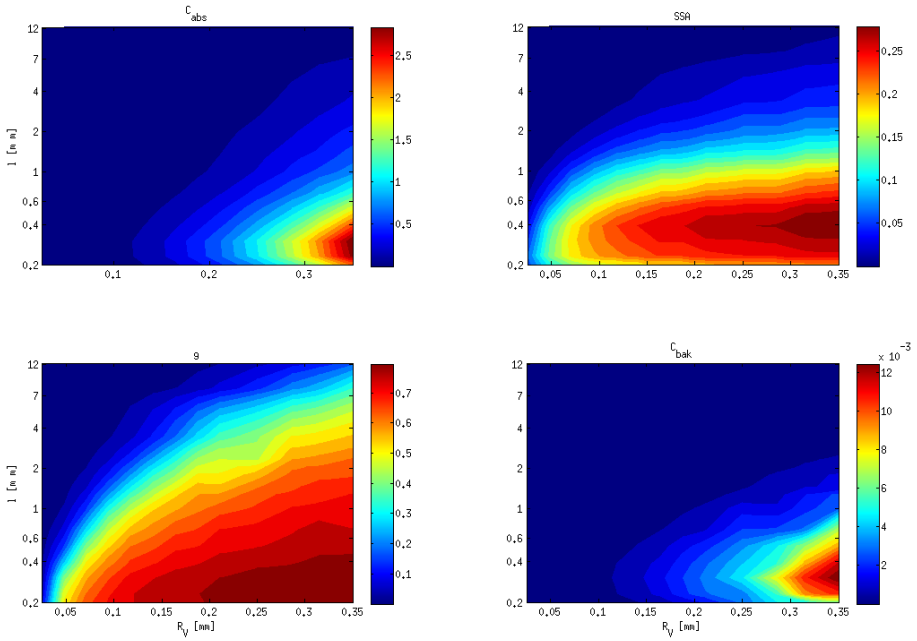

Figure 2. Absorption cross section C_{abs} (upper left), single-scattering albedo SSA (upper right), asymmetry parameter g (bottom left), and backscattering cross section C_{bak} (bottom right) of black carbon aggregates as a function of volume-equivalent radius R_V and wavelength λ.

GMDD
8, 10735–10781, 2015

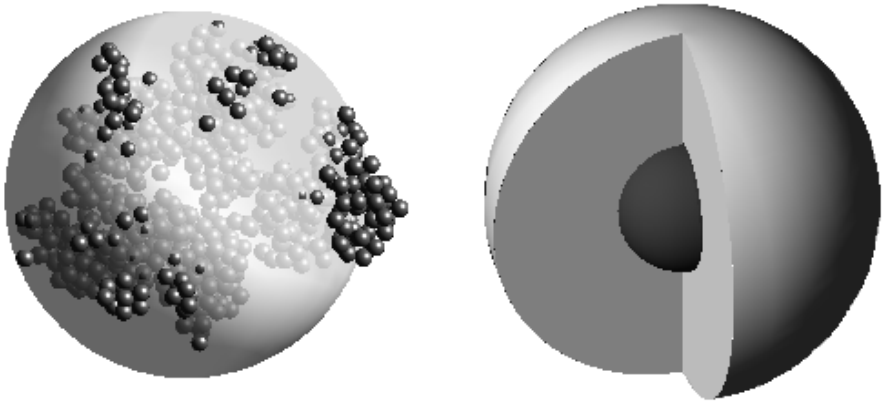

Figure 3. Morphologically realistic encapsulated aggregate model for internally mixed black carbon (left), and core-grey-shell model (right).

GMDD
8, 10735–10781, 2015

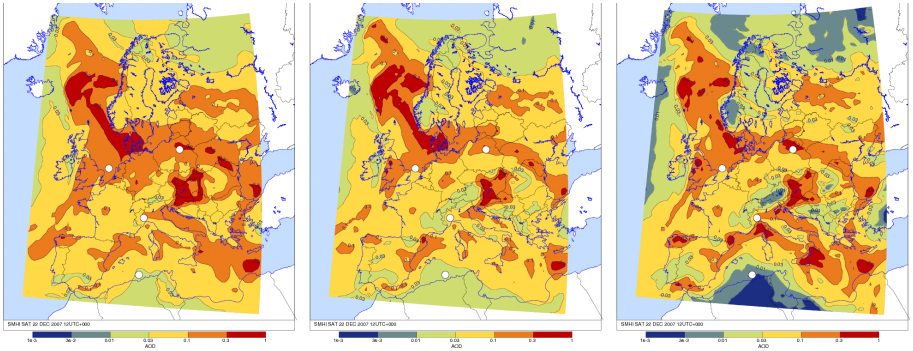

Figure 4. Aerosol optical depth over Europe on 22 December 2007, 12:00 UTC (noon). Results are shown for the mass transport model in conjunction with the old external-mixture optics model (left), and with the new internal-mixture/core-grey-shell/fractal BC aggregate model (center), as well as for the MATCH-SALSA model in conjunction with the new optics model (right). The circles indicate the four locations used for radiative transfer studies. Note the semi-logarithmic colour scale!

GMDD
8, 10735–10781, 2015

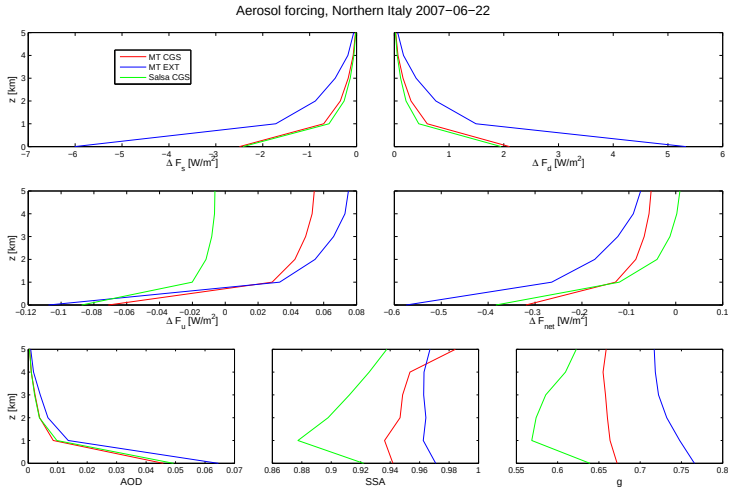

Figure 5. Aerosol forcing and optical properties at 532(CGS)/500(EXT) nm for Northern Italy in June.

GMDD
8, 10735–10781, 2015

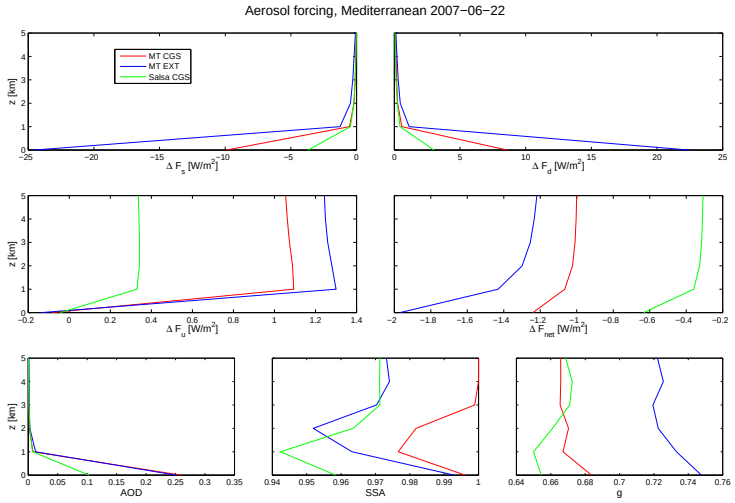

Figure 6. Aerosol forcing and optical properties at 532(CGS)/500(EXT) nm for the Mediterranean in June.

GMDD
8, 10735–10781, 2015

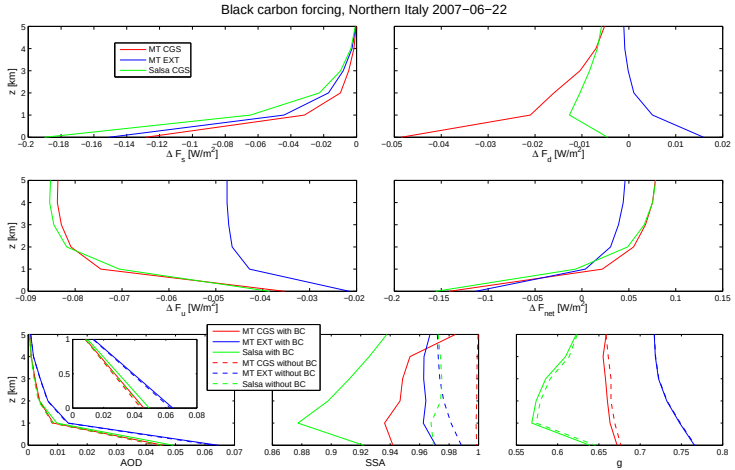

Figure 7. Black carbon forcing and optical properties at 532(CGS)/500(EXT) nm for Northern Italy in June.

GMDD
8, 10735–10781, 2015

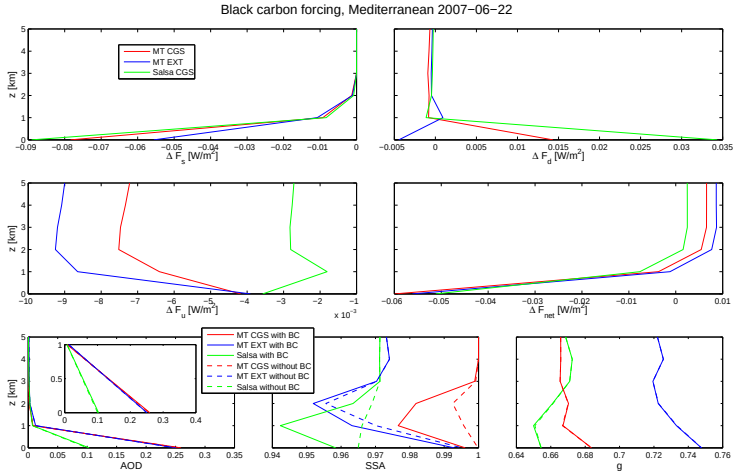

Figure 8. Black carbon forcing and optical properties at 532(CGS)/500(EXT) nm for the Mediterranean in June.

GMDD
8, 10735–10781, 2015

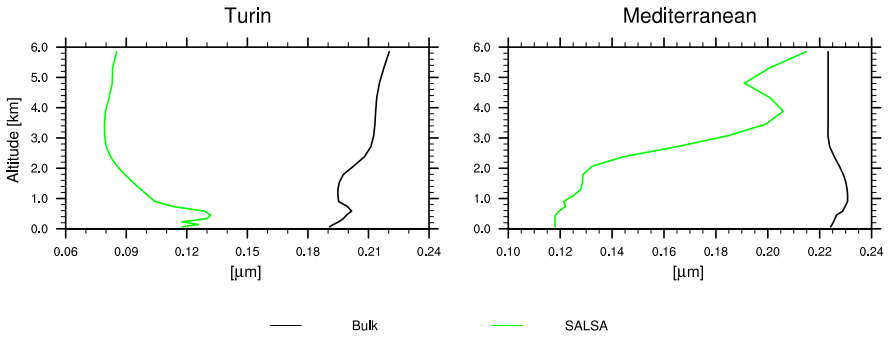

Figure 9. Effective radius for the two chemical transport model versions MT and SALSA over Northern Italy and Mediterranean in June.

GMDD
8, 10735–10781, 2015

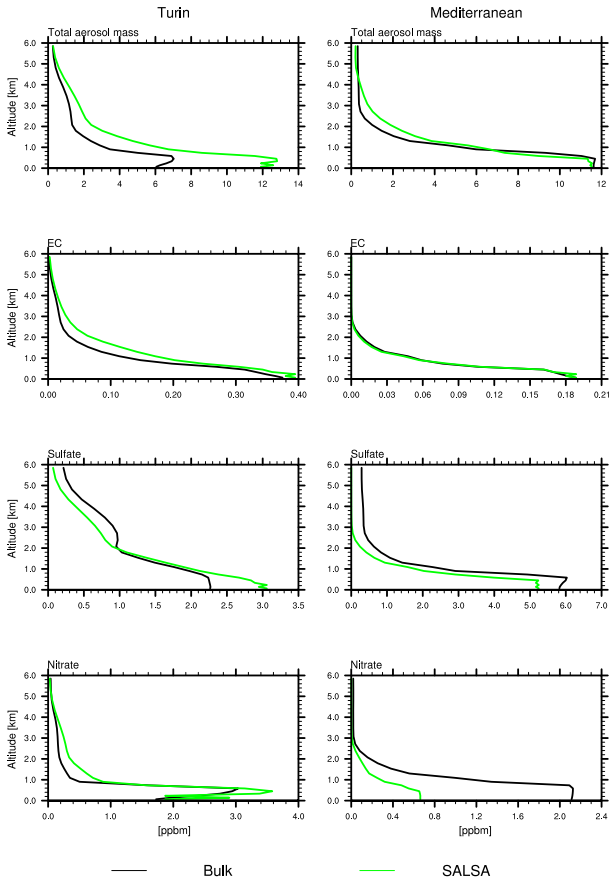

Figure 10. Vertical distribution of aerosols at Northern Italy and Mediterranean in June.

GMDD
8, 10735–10781, 2015

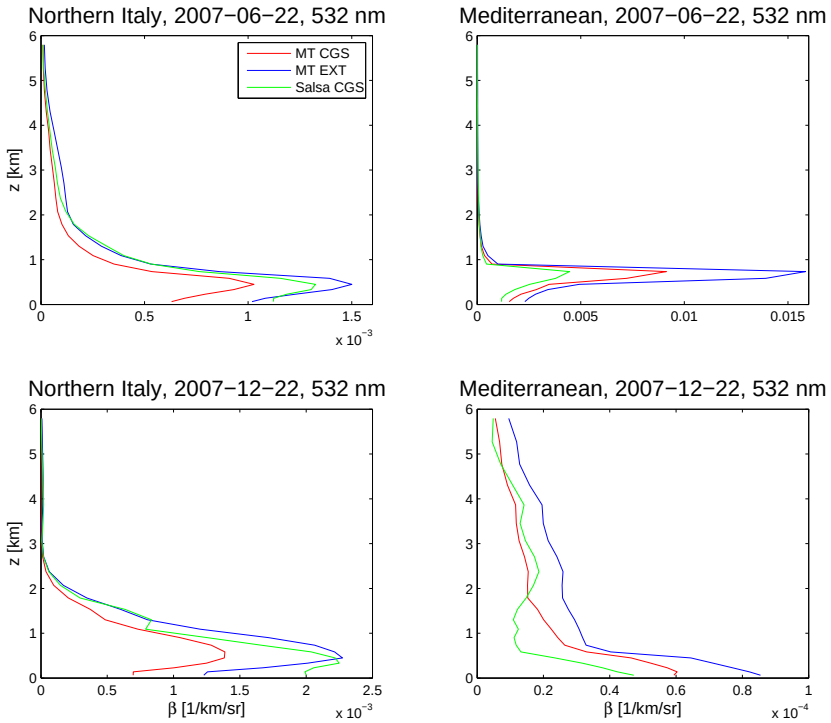

Figure 11. Backscattering coefficient at a wavelength of 532 nm at two different locations and at two different instances, computed with the three model versions.

GMDD
8, 10735–10781, 2015